EXPERIMENTAL AND NUMERICAL DETERMINATION OF PRESSURE AND VELOCITY DISTRIBUTION INSIDE A ROTOR-STATOR CAVITY AT VERY HIGH CIRCUMFERENTIAL REYNOLDS NUMBERS

B. Barabas, S. Clauss, S. Schuster, F.-K. Benra, H. J. Dohmen, D. Brillert

University of Duisburg-Essen, Chair of Turbomachinery, Duisburg, Germany,
botond.barabas@uni-due.de

ABSTRACT

For many future applications the discharge pressure of industrial radial compressors has to be strongly raised compared to the present situation. An upcoming application for high pressure compressors will be Carbon Capture and Storage technology.

The design of high pressure radial compressors strongly depends on the flow structure between the outer sides of the rotor disks and the casing walls. The flow structure inside these so called rotor-stator cavities affects the axial thrust of the machine and the friction at the outer sides of the disks in a significant way. Rotor-stator cavities have been investigated by many researchers experimentally and numerically in the past decades. However, investigations have been conducted for maximum circumferential Reynolds numbers smaller than 2.5×10^7. For described future applications, circumferential Reynolds numbers higher than 10^8 are estimated.

In order to close the knowledge gap about flow physics in rotor-stator cavities for highest Reynolds numbers a test rig has been designed and built up at the University of Duisburg-Essen. In this contribution, the novel test rig is described in detail and first measurement results are presented. Pressure data inside the cavity gained from experiments are compared to published experimental results. Preliminary CFD results with superposed flow at highest Reynolds numbers are presented and discussed.

NOMENCLATURE

A	m^2	Area	P	kW	Power
b	mm	Disk thickness	r	mm	Radius
c_m	–	Moment coefficient	R	mm	Disk outer radius
c_p	–	Pressure coefficient	Re_φ	–	Circumferential
D	mm	Disk diameter	s	mm	Axial gap width
F	N	Force	t	mm	Radial gap width
G	–	Non dimensional axial gap width	T	K	Temperature
i	–	Transmission ratio	T_q	Nm	Torque
Ma	–	Mach number	u	m/s	Circumferential velocity
n	$1/s$	Rotational speed	v	m/s	Velocity
p	N/m^2	Pressure			

INTRODUCTION

The flow inside rotor-stator cavities of radial compressors is highly complex and has a major impact on the operating performance. The axial thrust of the shaft is mainly driven by the pressure distribution in the side chambers and the drag torque is influenced by the flow pattern inside the chambers. Decades ago first experimental investigations have been conducted e.g. by Daily and Nece (1960), Kurokawa et al. (1972, 1976, 1978), and Petry et al. (2010). Daily and Nece (1960) set the reference in flow pattern investigations without superposed through-flow and established the division of the flow pattern inside a rotor-stator cavity into four different regions. The investigations have been performed for circumferential Reynolds numbers lower than 4×10^6. Recent experimental investigations up to $Re_\varphi = 2.5 \times 10^7$ with superposed through-flow and measuring the influence of obstacles have been conducted at the University of Sussex by Coren et al. (2009) and Long et al. (2012). However, the design of modern radial compressors is still based on these data, while the circumferential Reynolds numbers reach up to more than 10^8. An application field of radial compressors is the high pressure compression of carbon dioxide in CCS power plants.

A demand of radial compressors, operating at high circumferential Reynolds numbers in future, requests reliable experimental data for an efficient design process. At the Chair of Turbomachinery at the University of Duisburg-Essen a novel rotor-stator cavity test rig has been built up. The main goal of the test rig is to investigate the axial thrust, the drag torque, and the flow pattern inside the rotor-stator cavity. Experiments will be conducted with and without superposed through-flow at circumferential Reynolds numbers up to 5×10^8. The results will be used for the design process of future radial compressors and the validation of CFD calculations.

BOUNDARY CONDITIONS

Circumferential Reynolds number

The described test rig allows measurements of the flow pattern at very high circumferential Reynolds numbers. The circumferential Reynolds number Re_φ is defined in Eq. (1):

$$Re_\varphi = \frac{\rho \cdot \Omega \cdot R^2}{\eta} = \frac{\Omega \cdot R^2}{\nu} = \frac{u \cdot R}{\nu} \qquad (1)$$

Thus, high circumferential velocity u and low viscosity v of the test gas is needed to achieve this very high Reynolds number.

Friction Power / Power consumption

The required drive power is estimated with existing empirical correlations, given by Daily and Nece (1960) in Eq. (3) to (6). The moment coefficient can be calculated in dependency of the circumferential Reynolds number Re_φ and the non dimensional axial gap width G, as defined in Eq. (2). The main dimensions of the basic setup are illustrated schematically in Figure 1.
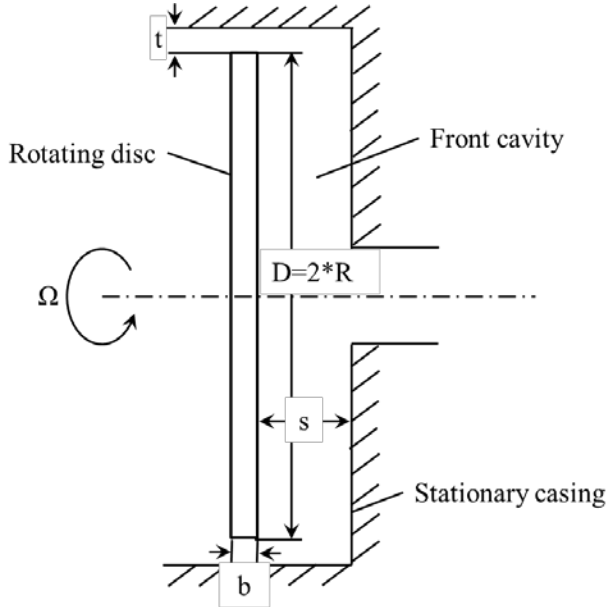
Figure 1: Rotor-stator disc cavity

$$G = \frac{s}{R} \tag{2}$$

Region I $\qquad\qquad c_{\text{m,DS}} = \dfrac{\pi}{G \cdot \text{Re}_\varphi}$ $\qquad\qquad\qquad\qquad\qquad$ (3)

Region II $\qquad\qquad c_{\text{m,DS}} = 1.85 \cdot G^{\frac{1}{10}} \cdot \text{Re}_\varphi^{-\frac{1}{2}}$ $\qquad\qquad\qquad$ (4)

Region III $\qquad\qquad c_{\text{m,DS}} = 0.04 \cdot G^{-\frac{1}{6}} \cdot \text{Re}_\varphi^{-\frac{1}{4}}$ $\qquad\qquad\quad$ (5)

Region IV $\qquad\qquad c_{\text{m,DS}} = 0.051 \cdot G^{\frac{1}{10}} \cdot \text{Re}_\varphi^{-\frac{1}{5}}$ $\qquad\qquad\quad$ (6)

Eq. (3) to (6) are valid for enclosed and hydraulically smooth disks in cavities without superposed flow. The different regions represent the laminar flow with (Region I) and without (Region II) merged boundary layers and the turbulent flow with (Region III) and without (Region IV) merged boundary layers (as shown in Figure 2).
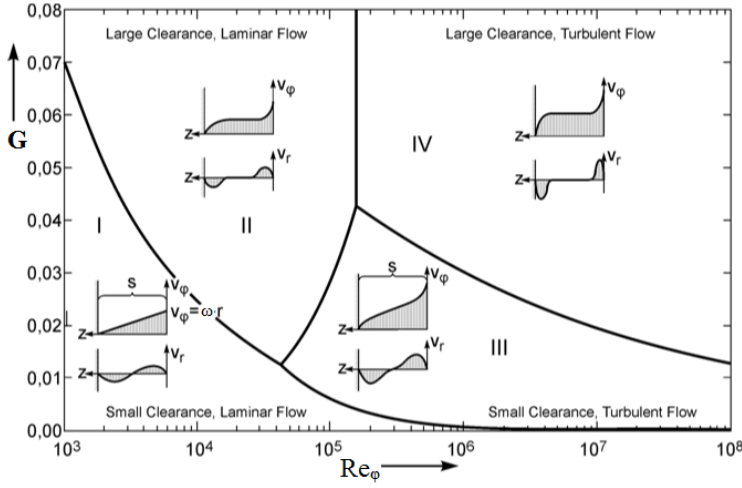
Figure 2: Flow regimes according to Daily and Nece (1960).

The highest friction losses occur with turbulent boundary layers, hence only flow regions III and IV are evaluated to determine the maximum power consumption of the test rig. The moment coefficient for the lateral surface of the disk is given by Bilgen and Boulos (1973) in Eq. (7), with t as the radial tip gap between rotor and casing.

$$\frac{c_{m,LS}}{b/R} = 0.204 \cdot \frac{(t/R)^{0.1}}{\mathrm{Re}_\varphi^{0.2}} \tag{7}$$

Eq. (7) is only valid for $\mathrm{Re}_\varphi \cdot t/R > 10^4$ and a concentrically enclosed cylinder without superposed flow.

$$T_{q,DS} = c_{m,DS} \cdot 0.5 \cdot \rho \cdot \Omega^2 \cdot r^5 \tag{8}$$

$$T_{q,LS} = c_{m,LS} \cdot 0.5 \cdot \rho \cdot \Omega^2 \cdot r^4 \cdot b \tag{9}$$

$$P_{total} = (2 \cdot T_{q,DS} + T_{q,LS}) \cdot \Omega \tag{10}$$

The friction power of this application, calculated with the existing empirical correlations and Eq. (8) to (10), yield values above 100 kW. The dependence between the achievable Reynolds number and the friction power is plotted in Figure 3. The influence of the fluid temperature is presented in the figure, as well. Furthermore, the effect of the axial gap width G on the friction power is shown. A wider gap dissipates more power than a narrow gap. The figure is normalized with the design values.

The required electrical drive power for the test rig is determined with the friction power of the disk, other losses (e.g. bearing and coupling losses), and additional friction power due to superposed flow. The superposed flow breaks up the core rotation inside the rotor-stator cavity and leads to higher friction losses.
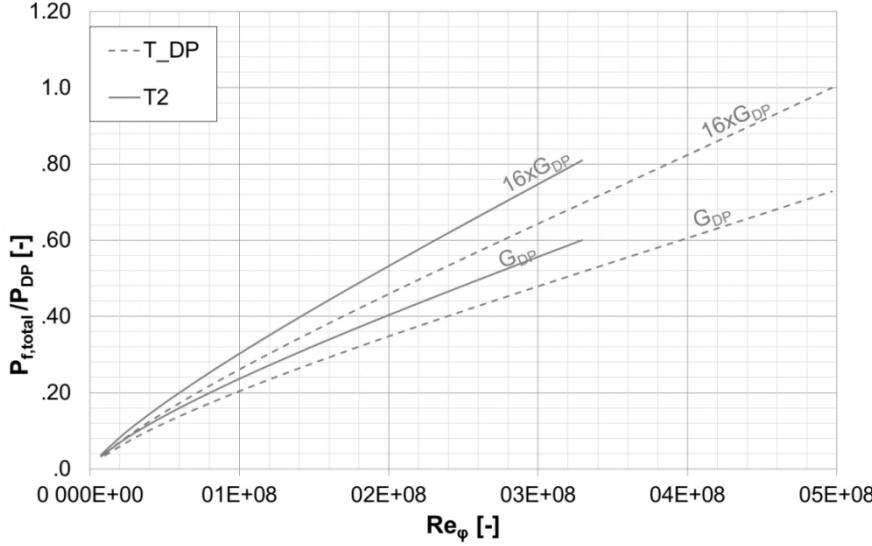
Figure 3: Normalized friction power $P_{f,total}/P_{DP}$ as a function of Reynolds number Re_φ for two different temperatures of the fluid.

Axial thrust

The axial thrust arising on the rotating disk and shaft is of vital importance for the bearing design. To get an estimate of the expected forces, the simplified radial equilibrium, shown in Eq. (11), is used, where ω refers to the angular velocity of the inviscid core. Assuming the core rotates as a solid body the radial equilibrium can be formulated as follows:

$$\frac{\partial p}{\partial r} = \rho \frac{u_\omega^2}{r} \quad \leftrightarrow \quad \frac{\partial p}{\partial r} = \rho \omega^2 r \tag{11}$$

The pressure field can be determined from Eq. (12). In order to solve the differential equation an incompressible flow is assumed.

$$\int_{p_1}^{p_2} dp = \int_{r_1}^{r_2} \rho \omega^2 r dr \rightarrow p_1 = p_2 - \rho \frac{(\beta\Omega)^2}{2} \cdot (r_2^2 - r_1^2) \text{ with } \omega = \beta\Omega \tag{12}$$

$$\int dF = \int p dA = \int p 2\pi r dr \tag{13}$$

$$\rightarrow F = \int_{r_i}^{R} \left(p_2 - \rho \frac{(\beta\Omega)^2}{2} (R^2 - r^2) \right) 2\pi r dr$$

$$\rightarrow F = \pi p_2 (R^2 - r_i^2) - \frac{\pi\rho(\beta\Omega)^2 R^2}{2}(R^2 - r_i^2) + \frac{\pi\rho(\beta\Omega)^2 R^2}{4}(R^4 - r_i^4) \tag{14}$$

$$\beta = \frac{1}{1+(1+t/R)^2\sqrt{(1+t/R)+5s/R}} \tag{15}$$

In Eq. (12) to Eq. (15) β describes the core rotation factor given by Zilling (1973), which is only valid without superposed flow. From Eq. (14) it can be seen that the axial thrust is caused by different core rotation factors of the front and rear cavity. These factors depend on the axial and radial gap width, which are set in accordance to the maximum axial thrust. The results are presented in Figure 4 for different rotational speeds. The parameters are normalized with their design point values.

5
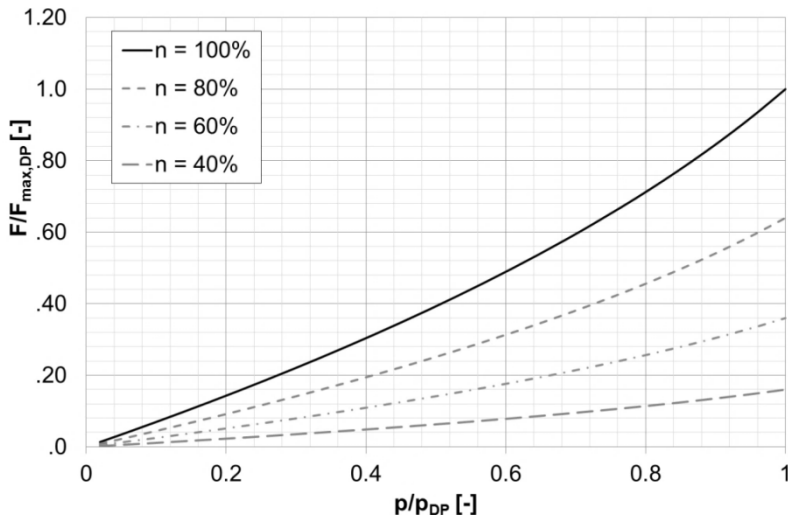
Figure 4: Non dimensional axial thrust $F/F_{max,DP}$ as a function of non dimensional pressure p/p_{DP} and rotational speed n.

MECHANICAL SETUP

The mechanical setup of the test rig includes a drive train with a continuously adjustable high speed motor. For torque control and accurate determination of the power, a torque measuring shaft with a relative accuracy of 99.9 % is integrated in the drive train. Taking into account the bearing losses, which are calculated using correlations of the manufacturer, we can determine very precisely the friction losses of the rotating disc. With regard to the desired high pressure and the filling medium carbon dioxide, the test rig is hermetically sealed.

For precise determination of the axial thrust, the fixed bearing unit is equipped with force measuring sensors. The accuracy of these sensors is 99.5 %. Due to power dissipation the housing covers are equipped with cooling chambers and cooling elements.

The design pressure of the test rig is above 20 bar. This fact combined with the large diameters lead to the complex design and the large material thickness of the components (as shown in Figure 5). Moreover, the casing has an exceptional geometric configuration that allows an easy variation of the dimensionless gap width G for both the rear and the front cavity. For a superposed flow in centripetal and centrifugal directions the casing is equipped with fittings connected to a compressor. To generate a pre-swirl for the superposed flow, changeable cylinders with vanes at the top of the rotating disk (centripetal) and near the hub (centrifugal) are provided.

Front cover

Rotating disk

Rear cover

Front cavity
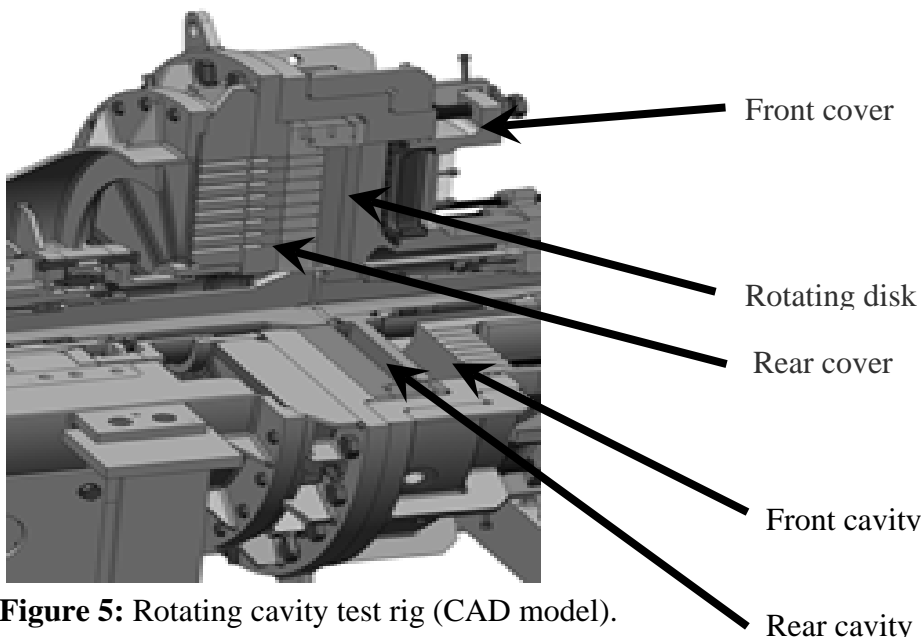
Figure 5: Rotating cavity test rig (CAD model).

Rear cavity

The circulation of the carbon dioxide is realized by means of a specially designed compressor, which compensates the pressure losses (pipeline, cavity, cooler) and the pumping action of the rotating disk. The hermetically sealed compressor has a design pressure ratio above $\pi = 1.15$, and is driven by a frequency converter controlled electric drive.

To investigate the flow structure inside the cavity, the front cover of the test rig is also equipped with several holes at different radial positions for the implementation of Hot-Wire-Anemometry (HWA) or multi-hole probes (MHP).

SAFETY CONCEPT

The high pressure and high kinetic power, stored in the rotor, demand a permanent monitoring and controlling of the following parameters: The bearing and winding temperatures of the electric drive and the bearing temperatures of the shaft are checked continuously. Furthermore, the vibrations of the bearings are examined permanently. The temperature at the embracing stator annulus cylinder is measured at two positions.

In Figure 6 the gas pressure control flowchart is presented. The filling line branch is equipped with the main block valve (V1), which regulates the gas supply. In case of emergency this valve can be accessed by an emergency button from outside the laboratory, too. A pressure reducing valve (V2) is located downstream of the main block valve (V1) to set the desired cavity pressure.
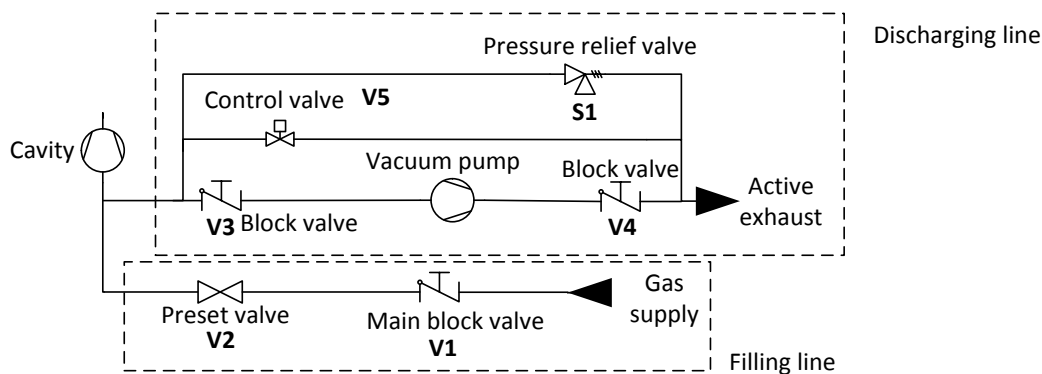
Figure 6: Gas pressure control flowchart.

The test rig discharging line is divided into three different branches. In the first of them a vacuum pump is located between two block valves (V3, V4). The vacuum pump is needed to evacuate the test rig before a defined gas mixture is filled into the cavity. The second line consists of the operational control valve (V5), which is used for the pressure regulation in normal operation and for the test rig discharge. The third branch is equipped with a safety valve (S1). In case of exceeding the set design pressure the valve opens. All three branches are connected to the main discharging line that exits the gas into the ambient with an active exhaust.

The usage of carbon dioxide in the test rig is another safety thread for humans. Therefore, the laboratory is equipped with three carbon dioxide sensors located near to the ground and connected to an alarm system. Although the test rig is designed without dynamic sealings, zero leakage cannot be assured. Furthermore, in the case of a mechanic failure, for instance of the viewing glass, the carbon dioxide expands instantly into the laboratory. Therefore the vent system of the laboratory is designed with a ten times air change within one hour. Together with the carbon dioxide sensors these assure a save environment for humans working in and in the near of the laboratory. The discharging lines, described in the last paragraph, are connected to this vent system, too.

MEASUREMENT POSITIONS

The positions for the scientific measurement equipment are presented in Table 1.

Type of measurement	Location	Number of positions	% disk radius	
			min	max
p and T	both chambers	8 positions	42	97
HWA	front chamber	5 positions	51	97

Table 1: Positions of the scientific measurements in the test rig.

CONVENTIONAL MEASUREMENTS

For the conventional temperature measurements 16 thermocouples of type K are used. The front and rear cavity are equipped with 8 thermocouples, respectively. The thermocouples are mounted in the housing, with their tips extended 2.5 mm into the cavity. The temperature of the casing can be taken as isothermal for the period of a measurement, due to its huge wall thickness and bad heat flux between the flow inside the cavity and the walls. Temperature compensation is performed within the data acquisition card.

The static wall pressure is measured through 1 mm bores in the casing wall at 8 radial positions in the front and rear cavity, respectively. A Scanivalve pressure acquisition system is used. The system allows a sequential measurement of the pressure channels with the same pressure sensor. Thus, an offset that would occur between different pressure transducers is avoided.

HOT WIRE ANEMOMETRY

The velocity measurements will be performed with HWA measurements. The HWA is an intrusive velocity measurement method, which means the flow is slightly disturbed by the probe.

The physical principle of the applied constant temperature anemometer (CTA) is a thin tungsten platinum coated wire (diameter: 3.8 µm) which is heated up to 250 °C. Its temperature is electronically controlled and hold at a constant level. Due to the forced convection, when the probe is placed in a flow, a flow velocity can be concluded. The bonding chain is the calibration of the probe that has to be performed at the same ambient conditions as the measurements are going to be done.

The HWA probes are going to be calibrated in a special calibration section of the superposed flow pipeline at different pressures and temperatures. The compressor flow can be bypassed around the cavity test rig only flowing through the calibration section in a closed loop. Temperature adjustments are achieved with a controlled in-line cooler.

The temperature correction of the HWA signal is going to be carried out in a two-step approach: First, the raw HWA signal is going to be measured for different radial and axial positions in the cavity. In the second step, the HWA probe is changed to a thermocouple and the temperatures are measured, while running a similar operation cycle, at respective radial and axial positions.

The HWA probe can be inserted at five different radial positions, as presented in Table 1. In Figure 7 the HWA probe is depicted. A single wire probe will be used; however a drawback of HWA is the unpredictable flow direction. The probe is mounted on a two-ax probe positioning system that allows an axial transition and a rotation of the probe. The accuracy of the probe positioning system is below 0.05 mm and 0.5 °. Measurements of the boundary layer up to a distance of 0.15 mm to the rotating disk have been performed and the position has been checked visually. The flow pattern inside the chamber is going to be expected transient and two dimensional, at least in the core region. In this case the flow direction can be detected with an extreme value search function that finds out the maximum value of the HWA signal, dependent on the rotation angle of the probe.
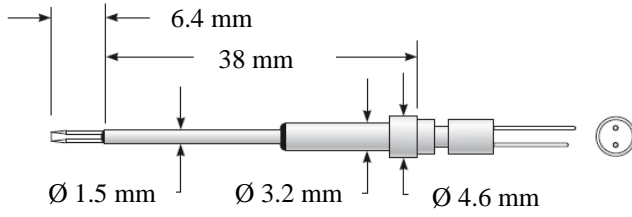
Figure 7: The applied hot wire probe according to TSI brochure.

EXPERIMENTAL VALIDATION

The validation of the radial pressure distribution of the test-rig has been performed in comparison to measured data by Radtke and Ziemann (1982) at Aachen University. The pressure coefficient $c_p(r)$ is defined in Eq. 16:

$$c_p(r) = \frac{p(R) - p(r)}{\rho \cdot \omega^2 \cdot R^2} \tag{16}$$

In Figure 8 the radial distribution of the pressure coefficients at equal circumferential Reynolds numbers ($Re_\Phi = 3.1 \times 10^6$) and zero through-flow with an axial gap width $G = 0.0625$ are compared with each other. The qualitative trend of the novel test rig data is in good accordance to the Aachen University data, both using smooth and plane disks. The maximum difference between the two measurements can be found in the outer region of the disk ($r/R \approx 0.95$) and is lower than one percent. Although, Radtke and Ziemann (1982) do not state in their report clearly which pressure is used for normalizing the pressures. The difference between both data decreases towards the disk's hub. Thus, the measured pressure data at the novel test-rig can reproduce former measurements in a different test rig. Further measurements of the velocity distribution inside the cavity have to be carried out to validate the HWA system.
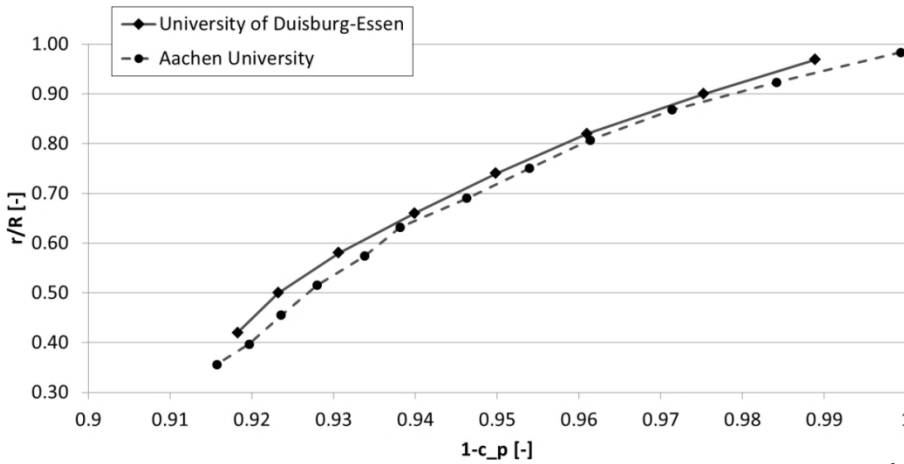
Figure 8: Comparison of pressure coefficients $c_p(r)$ at $Re_\Phi = 3.1 \times 10^6$ and zero through-flow gained at the University of Duiburg-Essen test-rig to the measured data at Aachen University (Radtke and Ziemann 1982).

In Figure 9 results of the radial pressure distribution in the cavity are presented. The axial gap width is kept constant and the circumferential Reynolds number has been varied. The curves of the pressure distributions seem to be similar at the hub ($r/R \approx 0.50$) and tip ($r/R \approx 1.0$) of the disk. However, in the middle region ($r/R \approx 0.80$) of the cavity the pressure distribution seems to show slight differences between the low Re_Φ and high Re_Φ results. These differences could be due to a different flow structure inside the cavity. Probably, the appearance of the boundary layers changed from the unseparated to the separated regime. Currently, the velocity profiles at high Reynolds

numbers are investigated to get a better insight into the flow mechanism taking place in the cavity and to extend the boundary line between flow regime III and IV up to Reynolds numbers above 1×10^8.
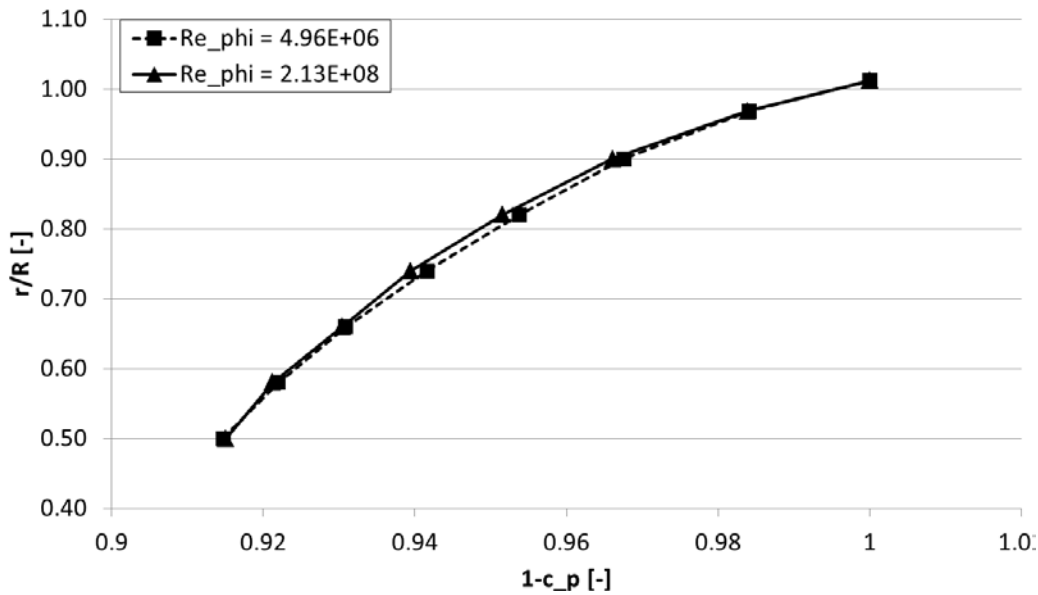
Figure 9: Comparison of pressure coefficients $c_p(r)$ at a constant axial gap width for different Re_Φ and zero through-flow.

NUMERICAL SIMULATION

In this paragraph, CFD calculations of the test rig are presented, which show the influence of pre-swirl vanes on the rotating flow inside the cavity.

The numeric calculation has been performed with Ansys CFX 14.0.

To account for real gas effects the gas properties are determined using the Peng-Robinson equation of state. The dynamic viscosity and conductivity are calculated with a kinetic theory model (Chung et al. 1984). To prevent heating of the fluid, the walls are calculated as diabatic, which corresponds to the cooled walls of the test rig.

A cross section of the computational domain is shown in Figure 10a). A one degree segment is meshed with a block structured grid and periodic boundary conditions are introduced. The y+ values of the mesh are below 50. Total pressure and total temperature are specified at the inlet upstream the pre-swirl vanes and the mass flow is specified at the exit. Spatial discretization is of second order accuracy for mass, momentum, and energy. For the turbulence transport equations a high resolution scheme is used. All calculations are performed as steady state. Turbulence effects are considered with the SST turbulence model in combination with scalable wall functions. The maximum residual is 10^{-6} and the percentage imbalance of mass, momentum, and energy is below 10^{-5}.

In Figure 10b) the pressure distribution of the numerical calculation is compared to two different experimental results gained in the Aachen test-rig (Radtke and Ziemann 1982). The data are gained at low circumferential Reynolds numbers of around 3.8×10^6 and zero through-flow. Measurement uncertainties are not given in the paper. The maximum deviation between the experimental values and the numeric data is below 1% and located around the middle of the disk ($r/R \approx 0.60$). The other regions show a better agreement. Thus for low Reynolds numbers the model can be considered as usable for further investigations.
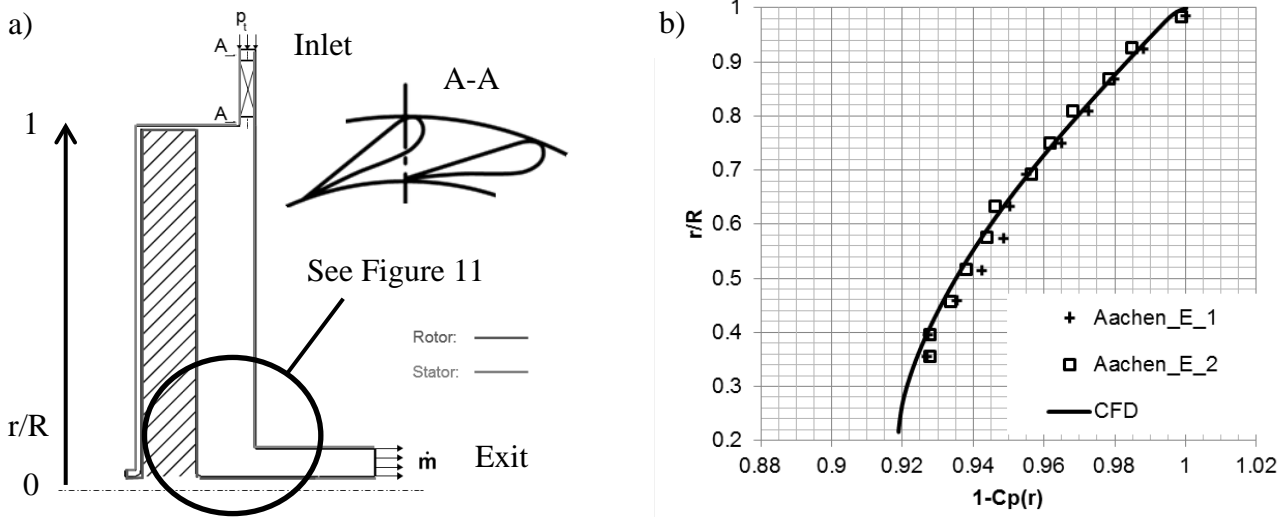
Figure 10: a) The computational domain of the cavity. b) The comparison between experimental data of the Aachen testrig (E_1 and E_2) and the CFD calculations. All data gained at zero through-flow and $Re\varphi = 3.8 \times 10^{6.}$

The computed radial distribution of static and total pressure for a high circumferential Reynolds number ($Re_\Phi = 1 \times 10^8$) is presented in Figure 11. The dynamic head of the pressure is decreasing from shroud ($r/R = 1$) towards hub ($r/R = 0.25$). The maximum dynamic pressure is obtained directly downstream of the pre-swirl vanes, which build up a high circumferential velocity component. In the main region of the cavity ($r/R \approx 0.9$ to $r/R \approx 0.3$) the static and total pressure are decreasing with nearly the same gradient. An obvious decline of the total pressure is present close to the hub region ($r/R \approx 0.25$), where the dynamic head is vanishing immediately.
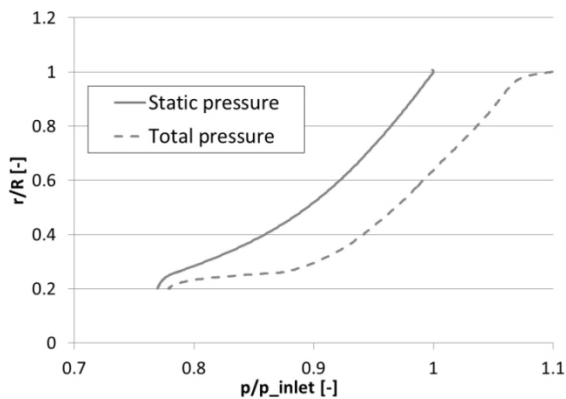
Figure 11: The radial distribution of the static and total pressure.

The explanation of this behavior might be an eddy that exists in the near hub region. In Figure 12 a close up view of this region, including the velocity vectors, is presented. The eddy near to the hub (I) rotates in clockwise direction and drives another eddy (II) in counter-clockwise direction. The mixing zone of both eddies ($r/R \approx 0.25$) causes the total pressure drop as shown in Figure 11.
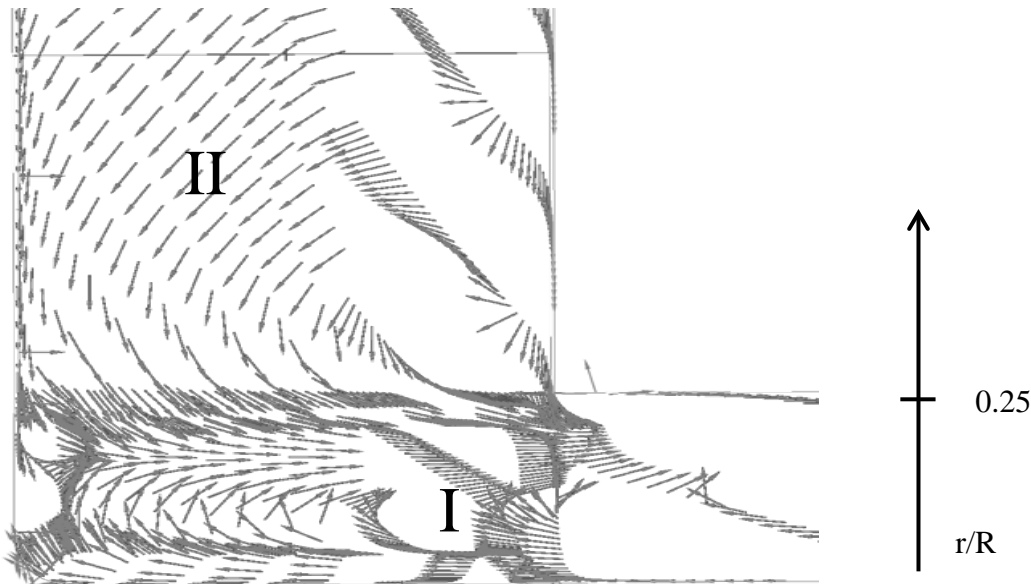
Figure 12: Close up view of the hub region with projected velocity vectors. (Detail of Figure 9 a)

SUMMARY AND OUTLOOK

This paper introduces a novel test rig, built up at the Chair of Turbomachinery at the University of Duisburg-Essen. It is designed for flow pattern investigations in rotor-stator cavities at very high Reynolds numbers. The design and safety concept of the test rig are thoroughly thought through, which allows a reliable operation of the test rig.

The first measurements of pressure data show good accordance to former experiments at low circumferential Reynoldsnumbers. The first results of the pressure distribution at high circumferential Reynolds number show the ability of the test rig to satisfy the expectations gathering data. Furthermore, the presented results give evidence that the boundary line between flow regimes III and IV has been crossed towards high Reynolds numbers. Current investigations of the velocity profile in the test rig are performed to confirm this assumption.

REFERENCES

Bayley F. J., Owen J. M. (1969): *Flow between a rotating and a stationary disc*, Aeronautical Quarterly, Vol. 20, pp. 333-354

Bilgen E., Boulos R. (1973): *Functional Dependence of Torque Coefficient of Coaxial Cylinders on Gap Width and Reynolds Number*, J. Fluids Eng., p. 122-126, ASME-Paper No. 72-WA/FE-1

Chung T.H., Lee L.L., Starling K.E. (1984): *Applications of Kinetic Gas Theories and Multiparameter Correlation for Prediction of Dilute Gas Viscosity and Thermal Conductivity*, Ind. Eng. Chem. Fundam., 23:8

Coren D., Childs P.R.N., Long C.A. (2009): *Windage sources in smooth-walled rotating disc systems*, Proceedings of the Institution of Mechanical Engineers, Part C: Journal of Mechanical Engineering Science, Vol. 223, No. 4, pp. 873-888

Daily J. W., Ernst W. D., Asbedian V. V. (1964): *Enclosed Rotating Discs with Superposed Through-Flow*, Massachusetts Institute of Technology, Report No. 64

Daily J. W., Nece R. E. (1960): *Chamber dimension effects on induced flow and frictional resistance of enclosed rotating discs*, Journal of Basic Engineering, 82, pp. 217-232

Kurokawa J., Sakuma M. (1988): *Flow in a Narrow gap along an Enclosed Rotating Disk with Through-Flow*, JSME International Journal, Series II, Vol. 31, No. 2, pp. 243-251

Kurokawa J., Toyokura T. (1972): *Study on Axial Thrust of Radial Flow Turbomachinery*, The Second International JSME Symposium Fluid Machinery and Fluidics, Tokyo, pp. 31-40

Kurokawa J., Toyokura T. (1976): *Axial Thrust, Disc Friction Torque and Leakage Loss of Radial Flow Turbomachinery*, International Conference on Pump and Turbine Design and Development, Vol. 1, Paper 5-2, Glasgow England

Kurokawa J., Toyokura T. (1978): *Roughness Effects on the Flow along an Enclosed Rotating Disc*, Bulletin of the JSME, Vol. 21, No. 162, Paper No. 162-8, pp. 1725-1732

Long C.A., Miles A. L., Coren D.D. (2012): *Windage Measurements in a Rotor Stator Cavity with Rotor Mounted Protrusions and Bolts*, Proceedings of ASME Turbo Expo 2012, Power for Land, Sea and Air, GT2012-69385, Copenhagen, Denmark

Owen J. M., Rogers R. H. (1989): *Flow and Heat Transfer in Rotating-Disc Systems*, Volume 1: Rotor-Stator Systems, Research Study Press, Taunton, Somerset, UK

Owen J. M., Pincombe J. R. (1980): *Velocity measurements inside a rotating cylindrical cavity with a radial outflow of fluid*, Journal of Fluid Mechanics, Vol. 99, No. 1, pp. 111-127

Petry N., Benra F., K., König S. (2010): *Experimental Study of Acoustic Resonances in the Side Cavities of a High-Pressure Centrifugal Compressor Excited by Rotor/Stator Interaction*, Proceedings of ASME Turbo Expo 2010, Power for Land, Sea and Air, GT2010-22054, Glasgow, UK

Radtke F., Ziemann M. (1982): Experimentelle und theoretische Untersuchungen des Reibungseinflusses an rotierenden Scheiben – Abschlussbericht, Aachen, Germany

Schlichting H. (1979): Boundary Layer Theory, McGraw-Hill, 7th edition

Schlichting H., Gersten K. (2006), Grenzschicht-Theorie, Springer-Verlag, Berlin, Germany

Will B. C., Benra F. K. (2008): *The Rise of Complexity in Describing Fluid Flow in Rotating Cavities*, Proceedings of FEDSM2008, ASME Fluids Engineering Conference, FEDSM2008-55341, Jacksonville, Florida, USA

Will B.C., Benra F. K. (2009): *Investigation of the Fluid Flow in a Rotor-Stator Cavity with Inward Through-Flow*, Proceedings of FEDSM2009, ASME Fluids Engineering Conference, FEDSM2009-78503, Vail, Colorado, USA

Will B. C., Benra F. K., Dohmen, H. J. (2010): *Numerical and Experimental Investigation of the Flow in the Side Cavities of a Centrifugal Pump*, The 12th International Symposium on Transport Phenomena and Dynamics of Rotating Machinery, ISROMAC 13-2010-0002, Honolulu, Hawaii, USA

Zilling H. (1973), *Untersuchung des Axialschubs und der Strömungsvorgänge in den Radseitenräumen einer einstufigen radialen Kreiselpumpe mit Leitrad, Mitt. d. Inst. Strömungslehre und Strömungsmaschinen*, Universität Karlsruhe, Vol. 15, p. 48